# Aeroelastic Stability of Aircraft with Circulation Control Wings

David J. Haas*
*David Taylor Research Center, Bethesda, Maryland*
and
Inderjit Chopra†
*University of Maryland, College Park, Maryland*

**The aeroelastic stability of aircraft with circulation control (CC) wings is examined. A beam finite element is used to model a high aspect ratio wing attached to a rigid fuselage. Unsteady aerodynamic loads on the wing are calculated using a linear, time-domain unsteady aerodynamic model based on the indicial response method. Steady experimental circulation control airfoil data are used to determine the airfoil lift curve slope and aerodynamic center location as a function of Mach number and blowing level. The results indicate that when a high level of blowing is applied, a "CC flutter" instability of the first wing bending mode can occur. If the blowing pressure ratio is held constant, the wing restabilizes at higher speed. With high blowing, the aircraft short-period mode also becomes unstable. The inclusion of rigid-body motion is shown to weaken the CC flutter instability due to inertia coupling of the wing elastic modes with the aircraft rigid-body motion.**

## Introduction

A TYPICAL circulation control (CC) airfoil is a quasi-elliptical airfoil in which lift is augmented and controlled by blowing a thin sheet of air through a slot near a rounded edge (Coanda effect); see Fig. 1. In the past, CC airfoils have been tested on rotary-wing,[1,2] fixed-wing,[3] and stoppable rotor aircraft.[4] Recently, a tail boom utilizing the circulation control concept became available on a light commercial helicopter in place of a conventional tail rotor as a means of reacting main rotor torque and providing directional control [no tail rotor (NOTAR) concept].[5]

Presently, the U.S. Navy is investigating a two-bladed stoppable rotor for an unmanned aerial vehicle (UAV).[6] The UAV can take off vertically in a rotary-wing mode and also loiter efficiently in a fixed-wing mode. The two blades in the stopped position form a high aspect ratio unswept wing. Dual slot CC airfoils (which have slots at both the leading and trailing edge) make the stoppable rotor concept feasible because they can operate efficiently with a relative wind approaching from either direction.

To date, most of the work in circulation control technology has focused on aerodynamic performance. Extensive testing of two-dimensional CC airfoils, CC fixed wings, and CC rotors have been performed at the David Taylor Research Center (DTRC).[7] A wind-tunnel test on an aeroelastically scaled model of a stoppable rotor aircraft with circulation control wings was conducted at the United Technologies Research Center, Hartford, Connecticut.[4] This test evaluated the aircraft in the X-wing mode and showed that a low-speed flutter instability exists for some combinations of angle of attack and blowing level.

Before CC airfoils can be safely introduced into modern aircraft designs, the aeroelastic behavior of wings with CC airfoils must be understood. Chopra[8] examined the aeroelastic stability of CC rotors and found appreciable differences in the stability results due to blowing as compared to conventional rotors. Recently, Haas and Chopra[9,10] have examined the effect of CC on the aeroelastic stability of fixed wings. The static nonlinear aeroelastic response of a CC wing is presented in Ref. 9.

In Ref. 10, the flutter characteristics of an isolated CC wing cantilevered at the root are presented. A flutter phenomenon, unique to CC airfoils, was identified. This phenomenon, termed "CC flutter," occurs at low angles of attack with high blowing. This analysis helped to explain the limit-cycle instability that has been observed in wind-tunnel tests of CC wings at certain angle-of-attack and blowing ranges. Also, it was shown in Ref. 10 that spanwise tailoring of the blowing distribution could be used to eliminate this flutter condition.

In earlier studies, Haas and Chopra[9,10] identified the unique aeroelastic characteristics of CC wings. The primary objective was to identify basic phenomena; therefore, investigations were carried out on a simple cantilevered wing (no rigid-body motion was allowed). Much of the present research on aircraft with forward-swept wings indicates the need to include aircraft rigid-body modes in the flutter analysis.[11-13] These studies have shown that the aeroelastic behavior of a free-free aircraft can be different from those of a cantilevered wing. For example, an aircraft with forward-swept wings can exhibit a low-frequency "body-freedom flutter" instability caused by a coupling of the wing-bending mode with the aircraft rigid-body pitch and plunge motions.

The objective of the present study is to extend this earlier work by including the effects of rigid-body motion on the CC flutter instability. Since CC flutter is primarily a bending-mode instability, it is expected that rigid-body freedom will have a significant influence on this instability. A flutter analysis is developed for an elastic wing attached to a rigid fuselage undergoing pitch and plunge motion about the center of gravity of the aircraft. The finite element method is used to discretize the elastic wing. A six-degree-of-freedom (DOF) beam-bending/torsion element is used to model the wing. The aircraft is assumed to be symmetric about its centerline so that only one-half of the aircraft is analytically modeled. Unsteady aerodynamic loads on the wing are calculated using a linear, time-domain, unsteady aerodynamic model based on indicial response functions. The airfoil static lift curve slope and aero-

Presented as Paper 89-1184 at the AIAA/ASME/ASCE/AHS/ASC 30th Structures, Structural Dynamics, and Materials Conference, Mobile, AL, April 3-5, 1989; received May 6, 1989; revision received Feb. 16, 1990. 

*Aerospace Engineer, Systems Department. Member AIAA.
†Professor, Department of Aerospace Engineering. Associate Fellow AIAA.

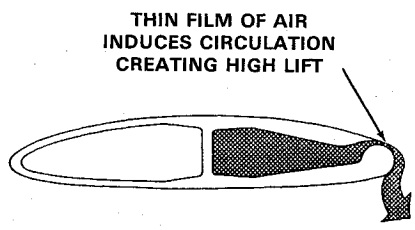


**Fig. 1 Typical circulation control airfoil.**

dynamic center location are obtained from experimental CC data. Aerodynamic loads on the horizontal tail (conventional airfoils) are calculated using quasisteady aerodynamics. The effects of several design parameters on CC flutter are investigated for both cantilevered wings and free-free aircraft.

## Circulation Control Aerodynamics

The aerodynamic forces generated by a circulation control airfoil arise from two sources: the angle of attack and the blowing level on the airfoil. The blowing level is characterized by a blowing momentum coefficient $C_\mu$ defined as:

$$C_\mu = (\dot{m}V_j/q_n c) \tag{1}$$

where $\dot{m}$ is the mass flow rate of air through the slot (per unit span), $V_j$ the calculated jet velocity assuming isentropic expansion to freestream pressure, $c$ the chord length, and $q_n$ the freestream dynamic pressure based on the velocity component normal to the wing leading edge. This coefficient is a basic performance parameter for CC airfoils.

For an aircraft with a circulation control wing, the jet momentum $\dot{m}V_j$ is produced by a compressor that supplies a duct pressure $P_d$ at the root of the wing. The ratio of duct pressure to freestream static pressure $P_d/P_\infty$ determines the jet momentum level. In this study, the compressor is assumed to provide a constant blowing pressure ratio with airspeed. Because the blowing momentum coefficient is nondimensionalized by dynamic pressure, $C_\mu$ will decrease as forward speed increases if the blowing pressure ratio is held constant. Because of compressor limitations, only relatively low values of $C_\mu$ can be obtained for Mach numbers above 0.5. Significant forces, however, can still be produced with blowing at high speeds due to the high level of dynamic pressure.

An alternate expression for $C_\mu$, valid for unchoked compressible flow, is

$$C_\mu = 2(h/c)(M_j/M)^2 \qquad \text{for } M_j < 1 \tag{2}$$

where $h/c$ is the slot height-to-chord ratio, $M_j$ the jet Mach number, and $M$ the freestream Mach number based on the velocity component normal to the leading edge of the airfoil. Comparing Eqs. (1) and (2), it can be seen that holding the blowing pressure ratio constant (and thus $\dot{m}V_j$ constant) is equivalent to maintaining a constant value of the quantity $C_\mu M^2$. For the examples in this paper, $C_\mu M^2$ is held constant at a value of $C_\mu M^2 = 0.004$, which represents a high level of blowing.

For a CC airfoil, lift can be divided into two components: angle-of-attack lift and blowing lift. Each of the components of lift is associated with a separate aerodynamic center. For angle-of-attack lift, the aerodynamic center is located near the quarter chord (similar to a conventional airfoil); for lift due to blowing, the aerodynamic center is located near the half chord. Figures 2a and 2b show lift and moment about the half chord for a typical CC airfoil at Mach = 0.3 for several values of blowing coefficient. (Generally, circulation control data are resolved at the half chord because the aerodynamic center associated with blowing is located near this position.) Note from Fig. 2 that the combined aerodynamic center can be located anywhere depending on angle of attack and blowing level.

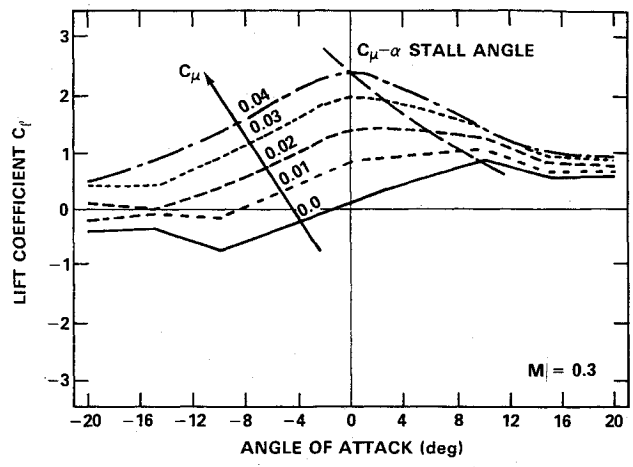


**a) Section lift coefficient**

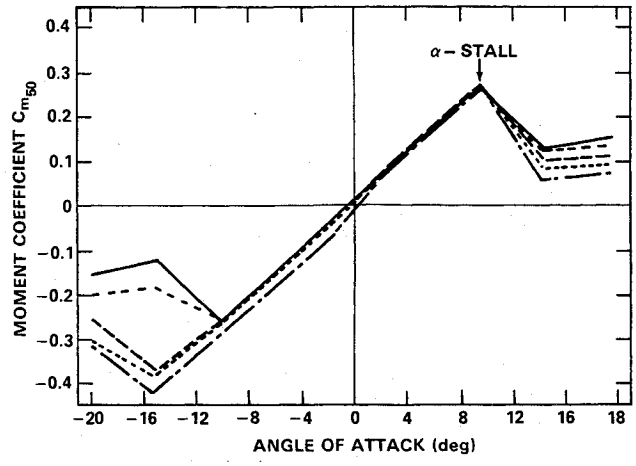


**b) Section moment coefficient about half chord**

**Fig. 2 Lift and moment data for typical CC airfoil.**

The data in Fig. 2 show two types of stall phenomena. The first type of stall is analogous to classical stall in that it is associated with flow separation at high angles of attack. This $\alpha$ stall is recognized by a change in sign of the slope of the half-chord pitching moment curve. This type of stall does not depend on the blowing level, and, for the present airfoil, $\alpha$ stall occurs at about 10 deg.

The second type of stall, $C_\mu$-$\alpha$ stall, occurs when blowing is present. The $C_\mu$-$\alpha$ stall is characterized by a change in sign of the lift curve slope with respect to angle of attack and occurs before $\alpha$ stall. The $C_\mu$-$\alpha$ stall condition is the result of a decrease in boundary-layer control effectiveness due to a thickening of the airfoil boundary layer as angle of attack is increased. When this occurs, the component of lift produced by blowing decreases rapidly as $\alpha$ is increased such that there is a net decline in total lift and, hence, stall. There is little or no change in the pithing moment about the half chord. The angle of $C_\mu$-$\alpha$ stall depends on the blowing level and typically (depending on airfoil thickness ratio and $C_\mu$ level) decreases as blowing is increased.

For the airfoil used in this study, the $C_\mu$-$\alpha$ stall range extends from about 0 to 10 deg (at $M = 0.3$), as shown in Fig. 2a. At 10 deg, $\alpha$ stall occurs and the flow separates regardless of the blowing level. At higher Mach numbers, the available $C_\mu$ is reduced and the curves tend to collapse onto the zero-blowing curve. Also, the $\alpha$ stall angle decreases as Mach number increases. These two effects narrow the range of angle of attack for $C_\mu$-$\alpha$ stall at higher Mach numbers.

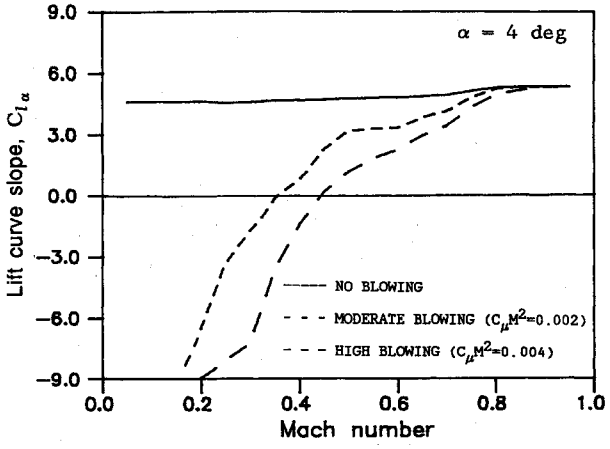


**Fig. 3 Variation of lift curve slope with Mach number.**

Figure 3 shows the variation in lift curve slope with Mach number for an airfoil at 4-deg angle of attack with no blowing, moderate blowing, and high blowing. At low Mach number, the airfoil is in the $C_\mu$-$\alpha$ stall range and the lift curve slope is negative when sufficient blowing is applied. However, if the Mach number is greater then 0.5, the lift curve slope remains positive up to the maximum blowing level. Operating in the $C_\mu$-$\alpha$ stall range is possible because of the gradual stall characteristics of CC airfoils. It should be noted that Reynolds number effects on lift curve slope are significant for CC airfoils because of the bluff trailing edge. These effects tend to cancel the well-known effect of compressibility on lift curve slope. This can be seen in Fig. 3, which shows that the lift curve slope is nearly constant with Mach number for the unblown airfoil. A more detailed description of CC aerodynamics and its applications is found in Refs. 14–16.

An extensive two-dimensional, steady CC airfoil data base is available at DTRC that contains airfoil characteristics over a broad range of Mach number, angle of attack, thickness-to-chord ratio, and blowing level. As seen in Fig. 2, these data are nonlinear with angle of attack and blowing level. At present, no unsteady CC airfoil data are available. However, analytical investigations have shown that Theodorsen-type unsteady aerodynamics may be applied for CC airfoils if the reduced frequency is moderate to low.[17]

Haas and Chopra[10] examined the low-speed aeroelastic stability characteristics of CC wings using a modified strip method[18] based on Theodorsen unsteady aerodynamic theory. This unsteady theory is formulated in the frequency domain, which restricts its applicability to simple harmonic motion. Thus, the analysis was only valid where the total system damping was equal to zero. In addition, compressibility effects were not accounted for. To overcome these deficiencies in the earlier analysis, a linear, time-domain, compressible, unsteady aerodynamic model based on the indicial response method is used in the present study.

## Unsteady Aerodynamics Model

The unsteady aerodynamic model is an eight-state, time-domain model based on the indicial method. This aerodynamic model (from Ref. 19) has been validated with experimental data to predict accurate unsteady aerodynamic loads on conventional airfoils up to transonic Mach numbers. Recently, this aerodynamic model was used to calculate flutter speeds on a two-dimensional wing.[20] Correlation with experimental data and complex computational fluid dynamic solutions showed that the state-space model predicted accurate flutter boundaries up to a Mach number of 0.875.

The indicial response functions used in the unsteady aerodynamic model are valid for an airfoil with attached flow. For a CC airfoil, the flow generally remains attached to the airfoil up to the point of $\alpha$ stall, even though the lift behaves as if the airfoil were stalled beyond the angle of $C_\mu$-$\alpha$ stall (i.e., decreasing lift with increasing $\alpha$). Since the flow remains attached, the use of linear unsteady aerodynamics is assumed to be applicable in the $C_\mu$-$\alpha$ stall region. Because an unsteady CC airfoil representation does not exist, no attempt was made to account for any unsteady jet effects due to perturbations in angle of attack. When experimental or analytical data become available, the necessary correction for these effects should be determined.

The indicial response functions are exponential functions of the form:

$$\phi(t,M) = 1 - A_1 e^{-b_1 t} - A_2 e^{-b_2 t}$$

$$\phi(t,M) = A_3 e^{-b_3 t}$$

The coefficients and time constants were determined by fitting unsteady experimental data for the NACA 0012 airfoil but can be adjusted for different airfoils if data exist. In addition, the steady lift curve slope and aerodynamic center location for the airfoil are required. Circulation control aerodynamics is introduced into the analysis by using the experimental values for the lift curve slope and aerodynamic center location at a given blowing level, Mach number, and angle of attack. In this way, the static, nonlinear behavior of CC airfoils can be accounted for using a linear, unsteady aerodynamic model.

The indicial response functions are used to calculate the normal force and pitching moment about the quarter chord due to a step change in angle of attack $\alpha$ and nondimensional pitch rate $q$ about the quarter chord. The indicial forces and moments have been divided further into circulatory and noncirculatory (impulsive) components. The noncirculatory loading can be thought of as analogous to the incompressible apparent mass terms used in the modified strip theory of Ref. 18. The aerodynamic lift and pitching moment coefficients can be written in terms of the indicial response functions as:

$$C_L(t,M) = \left[C_{l_\alpha}\phi^C_\alpha(t,M) + 4/M\phi^I_\alpha(t,M)\right]\alpha + \left[C_{l_\alpha}/2\phi^C_q(t,M) + 1/M\phi^I_q(t,M)\right]q \tag{3a}$$

$$C_{M_{1/4c}}(t,M) = \left[-1/M\phi^I_{\alpha M}(t,M)\right]\alpha + \left[-C_{l_\alpha}/16\phi^C_{qM}(t,M) - 7/(12M)\phi^I_{qM}(t,M)\right]q + \left[C_{l_\alpha}\phi^C_\alpha(t,M)(1/4 - \chi_{ac}(M)\right](\alpha + q/2) \tag{3b}$$

where $\phi^C_\alpha$, $\phi^I_\alpha$, $\phi^C_q$, $\phi^I_q$, $\phi^I_{\alpha M}$, $\phi^C_{qM}$, and $\phi^I_{qM}$ are the indicial response functions, which are functions of both time and Mach number. Superscripts $C$ and $I$ on the indicial functions refer to the circulatory and impulsive loading, respectively.

By application of the Laplace transform to the indicial response, the unsteady aerodynamic system can be expressed in the state-space form.[20] In this form, Eqs. (3a) and (3b) represent a two-input/two-output feedback system with the state equations:

$$\dot{x} = Ax + B\begin{Bmatrix}\alpha\\ q\end{Bmatrix} \tag{4}$$

and output equation:

$$\begin{Bmatrix}C_L\\ C_M\end{Bmatrix} = Cx + D\begin{Bmatrix}\alpha\\ q\end{Bmatrix} \tag{5}$$

The vector $x$ is an $8 \times 1$ vector of aerodynamic state variables, and $A$, $B$, $C$, and $D$ are matrices of aerodynamic coefficients. The aerodynamic loads on a two-dimensional airfoil due to any arbitrary time history of $\alpha$ and $q$ can be determined by integration of Eqs. (4) and (5).

In order to apply the prior two-dimensional unsteady aerodynamic model in a general aeroelastic analysis program, the

lift and pitching moment about the elastic axis due to pitch and plunge motions are derived. Summing the forces and moments on the airfoil at the elastic axis yields

$$\begin{Bmatrix} C_L \\ C_{M_{ea}} \end{Bmatrix} = \begin{Bmatrix} C_L^C + C_L^I \\ C_L^C(0.5 + a_{ea}/2 - \chi_{ac}) + C_L^I(0.25 + a_{ea}/4) + C_M^C + C_M^I \end{Bmatrix} \tag{6}$$

where $\chi_{ac}$ is the aerodynamic center location from the leading edge (nondimensionalized by chord length) and $a_{ea}$ is the elastic axis location aft of the half chord (nondimensionalized by semichord). A transformation is required to express $\alpha$ and $q$ in terms of pitch and plunge motion at the elastic axis. This transformation is:

$$\begin{Bmatrix} \alpha \\ q \end{Bmatrix} = \begin{bmatrix} 0 & 1 \\ 0 & 0 \end{bmatrix} \begin{Bmatrix} w \\ \theta \end{Bmatrix}_{ea} + \begin{bmatrix} -1/V & -0.5c/V(0.5 - a_{ea}) \\ 0 & c/V \end{bmatrix} \begin{Bmatrix} \dot{w} \\ \dot{\theta} \end{Bmatrix}_{ea} \tag{7}$$

where the superscript (˙) indicates the derivative in time. By combining Eqs. (4–7), the lift and pitching moment about the elastic axis can be obtained for any arbitrary pitch and plunge motion of the airfoil about its elastic axis.

## Finite Element Formulation

The aeroelastic equations of motion for the aircraft are derived using the finite element method based on the Lagrange equations. A two-node, six DOF beam finite element is used to model the elastic wing. Continuity of bending displacement, bending slope, and elastic twist angle is maintained between elements. The fuselage is allowed to pitch and plunge about the aircraft center of gravity (CG). Since body motions that are symmetric with respect to the aircraft's centerline are considered, only one-half of the aircraft is modeled. Figure 4 shows a schematic of the analytical model used.

The wing is coupled to the fuselage by the constraint equation:

$$\begin{Bmatrix} q_1 \\ q_2 \\ q_3 \end{Bmatrix}_{\substack{\text{wing} \\ \text{root}}} = \begin{bmatrix} 1 & y_w \\ 0 & -\sin\Lambda \\ 0 & \cos\Lambda \end{bmatrix} \begin{Bmatrix} w \\ \theta \end{Bmatrix}_{\text{aircraft CG}} \tag{8}$$

where $q_1$, $q_2$, and $q_3$ are the first three degrees of freedom of the element attached to the fuselage. In the absence of external aerodynamic forces, the element stiffness and mass matrices are assembled with the fuselage terms to yield the equations of motion:

$$M\ddot{q} + Kq = 0 \tag{9}$$

The natural vibration modes are calculated from Eq. (9).

Aerodynamic forces are applied to the aircraft by the wing and horizontal tail. The effects of body aerodynamics, wing-body interaction, wing-tail interaction, and finite wing span are neglected. The element force vector is determined from the principle of virtual work using an aerodynamic strip theory approach. The total external work $\delta W$ is

$$\delta W = \delta W_t + \delta W_w \tag{10}$$

where $\delta W_t$ and $\delta W_w$ are the tail and wing components, respectively. The $\delta W_w$ represents a summation over all elements of the wing. Integration over the element length is carried out numerically using a one-point Gauss quadrature rule. Thus,

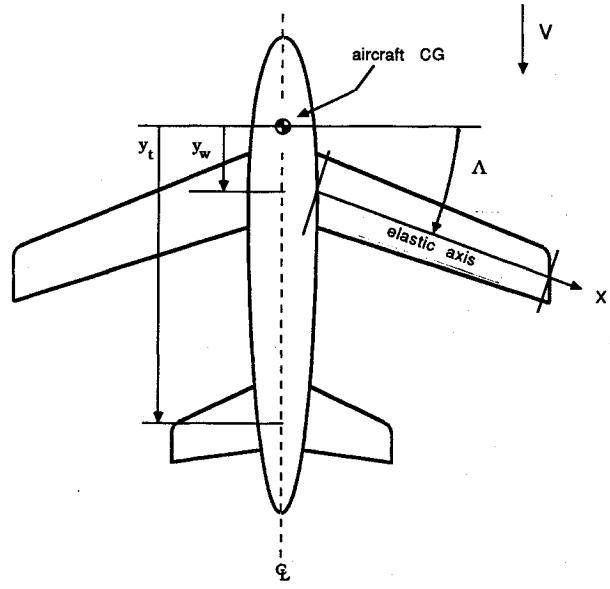


**Fig. 4 Planform geometry of aircraft model.**

each finite element has six structural DOF and eight aerodynamic states associated with it.

In order to evaluate the element force vector, the aerodynamic lift and moment must be calculated at each Gauss point. In the previous section, the aerodynamic forces and moments were expressed in terms of the airfoil pitch and plunge motions and an aerodynamic state vector $x$. Equation (7) can be expressed in terms of element nodal displacements as

$$\begin{Bmatrix} \alpha \\ q \end{Bmatrix} = A_1 q_e + A_2 \dot{q}_e \tag{11}$$

Equation (11) includes a correction for sweep effects such that the increment in $\alpha$ due to sweep is

$$\Delta\alpha(x) = -\frac{\partial w(x)}{\partial x}\tan\Lambda$$

Following the aerodynamic strip theory approach, the aerodynamic lift and moment per unit length is expressed as

$$\begin{Bmatrix} L \\ M_{ea} \end{Bmatrix} = q_n c \begin{bmatrix} 1 & 0 \\ 0 & c \end{bmatrix} \begin{Bmatrix} C_L \\ C_{Mea} \end{Bmatrix} = A_0 \begin{Bmatrix} C_L \\ C_{Mea} \end{Bmatrix} \tag{12}$$

Combining Eqs. (5), (11), and (12), the general expression for the aerodynamic loads can be written as

$$\begin{Bmatrix} L \\ M_{ea} \end{Bmatrix} = \left[A_0 C\right] x_e + \left[A_0 D A_1\right] q_e + \left[A_0 D A_2\right] \dot{q}_e \tag{13}$$

where $x_e$ is the vector of aerodynamic states associated with a given element. Integration of Eq. (13) yields the element generalized force vector:

$$Q_e = F_e x_e + K_a q_e + C_a \dot{q}_e \tag{14}$$

The aerodynamic state equation for the element can be written by combining Eqs. (4) and (11):

$$\dot{x}_e = A x_e + [BA_1] q_e + [BA_2] \dot{q}_e \tag{15}$$

Assembling Eqs. (14) and (15) over each of the elements yields a global force vector and the aerodynamic state equations for the entire aircraft. Using the Lagrange equations, the

aeroelastic equations for the aircraft can be written as

$$M\ddot{q} + Kq = Q \tag{16a}$$

$$\dot{x} = Ax + G_1 q + G_2 \dot{q} \tag{16b}$$

where

$$Q = Fx + K_a q + C_a \dot{q} \tag{16c}$$

Matrices that are not given explicitly can be found in Ref. 16.

Equations (16a–16c) are reduced into modal space by assuming a solution to Eq. (16a) of the form

$$q = \Phi z \tag{17}$$

where $\Phi$ is a matrix whose columns are the mode shapes determined from an eigenvalue analysis of Eq. (9) and $z$ is the reduced vector of modal DOF. For flutter analysis, only a few selected modes are required. Substituting Eq. (17) into Eqs. (16a–16c) and placing the resulting equation into first-order state-space form yields

$$\begin{bmatrix} I & 0 & 0 \\ 0 & \bar{M} & 0 \\ 0 & 0 & I \end{bmatrix} \begin{Bmatrix} \dot{z} \\ \ddot{z} \\ \dot{x} \end{Bmatrix} = \begin{bmatrix} 0 & I & 0 \\ (\bar{K}_a - \bar{K}) & \bar{C}_a & \bar{F} \\ \bar{G}_1 & \bar{G}_2 & A \end{bmatrix} \begin{Bmatrix} z \\ \dot{z} \\ x \end{Bmatrix} \tag{18}$$

where the modal matrices are denoted with bars.

Equation (18) is solved as an algebraic eigenvalue problem and each eigenvalue is represented as

$$p = \sigma + \iota\omega$$

The critical damping ratio $\zeta$ for each mode can be determined as:

$$\zeta = -\sigma/\sqrt{\sigma^2 + \omega^2} \tag{19}$$

and the frequency of oscillation is $\omega$. A plot of frequency and damping vs airspeed is compiled by solving for the eigenvalues at each velocity increment. An instability occurs when the total damping ratio becomes less than zero (i.e., damping ratio is negative). If structural damping is included, an instability condition occurs when the value of $\zeta$ calculated from Eq. (19) just equals the amount of structural damping available in that structural mode. Because a time-domain, unsteady aerodynamic model is used, the eigenvalue solutions are valid at the flutter condition (total damping = 0) as well as away from the flutter condition.

## Results and Discussion

For numerical results, properties of a typical stoppable rotor aircraft design are used. The wing is assumed to be uniform with a semispan $R$ equal to 30 ft and an aspect ratio of 10. The ratio of wing torsion-to-bending frequency is 10.0, which is larger than that of a conventional wing. The elastic axis and wing center of gravity are located at the half-chord position. The wing has a 17% quasi-elliptical CC airfoil with blowing near the trailing edge. The fuselage is also chosen to be representative of this class of aircraft. For the baseline configuration, the vehicle gross weight is 15,000 lb, which results in a ratio of wing mass to fuselage mass of 0.09. The wing is attached to the fuselage at a distance $0.1R$ aft of the aircraft CG. A horizontal tail with conventional airfoils and an area of one-tenth the wing area is located at a distance of $1.1R$ aft of the aircraft CG. Table 1 summarizes the properties of the baseline aircraft. The first three elastic wing modes (two bending and one torsion) are used in the analysis, and structural damping is set to zero.

**Table 1 Properties of baseline aircraft configuration**

| | |
|---|---|
| Wing semispan, $R$ | 30 ft |
| Wing chord, $c$ | 3 ft |
| Wing location, $y_w$ | 3 ft |
| Wing sweep, $\Lambda$ | 0 deg |
| Tail area | 9 ft$^2$ |
| Tail location, $y_t$ | 33 ft |
| Aircraft mass | 466 slugs |
| Aircraft pitch inertia, $I_{fo}$ | 34,237 slug-ft$^2$ |
| Airfoil | 17% quasi-elliptic |
| Slot location | 0.97c |
| Slot, $h/c$ | 0.0015 |

To gain an understanding of the basic aeroelastic characteristics of the wing used, stability results are calculated for the wing cantilevered at the root (no rigid-body motion). Figure 5 shows the frequency and damping trends vs velocity for the first bending (1B) and first torsion (1T) modes of the unswept wing at 4-deg angle of attack with no blowing. For this configuration, the first torsion mode has nearly zero damping at low velocity and then becomes stable as velocity increases. Inherent structural damping in the wing will ensure the stability of this mode at low velocity. The first torsion and bending modes are well separated such that coupling between these modes is weak, and the wing remains stable for all velocities shown.

The results for the cantilevered wing are repeated at the same angle of attack but with a high blowing level, $C_\mu M^2 = 0.004$; see Fig. 6. This combination of angle of attack and blowing level is chosen for this and subsequent examples because it corresponds to a range of $\alpha$ and $C_\mu$ where a $C_\mu$-$\alpha$ stall condition exists at low Mach numbers. The combination

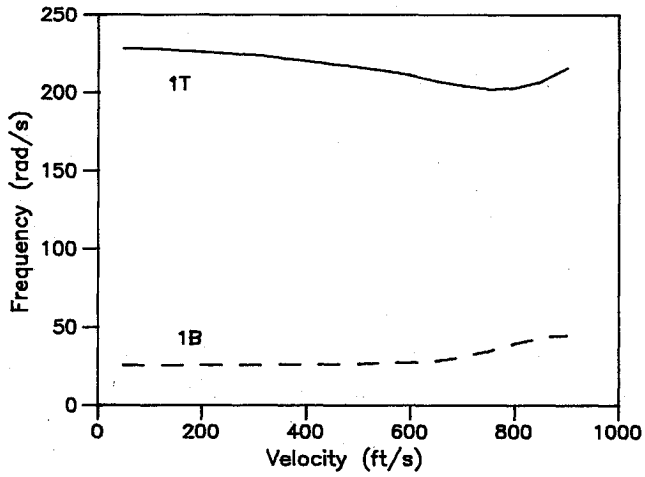


a) Frequency

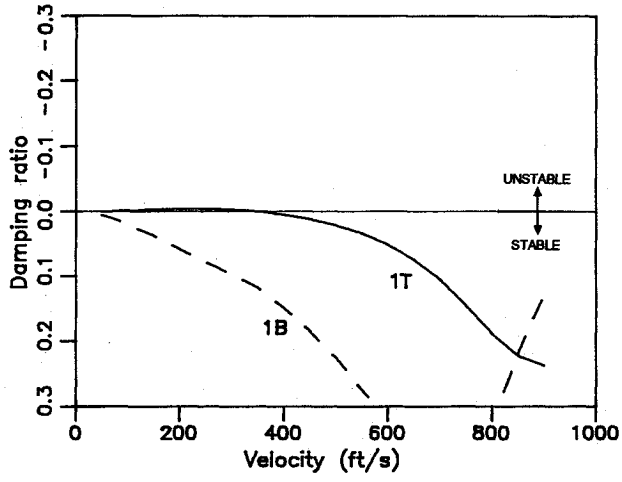


b) Damping ratio

Fig. 5 Cantilevered wing with no blowing.

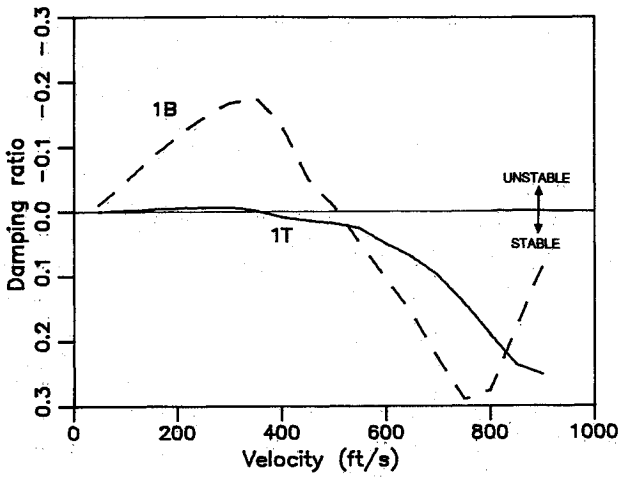


Fig. 6 Damping ratio for cantilevered wing with high blowing.

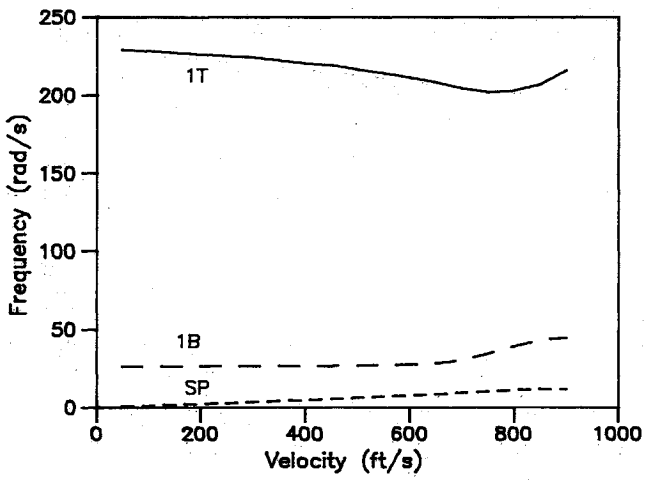


a) Frequency

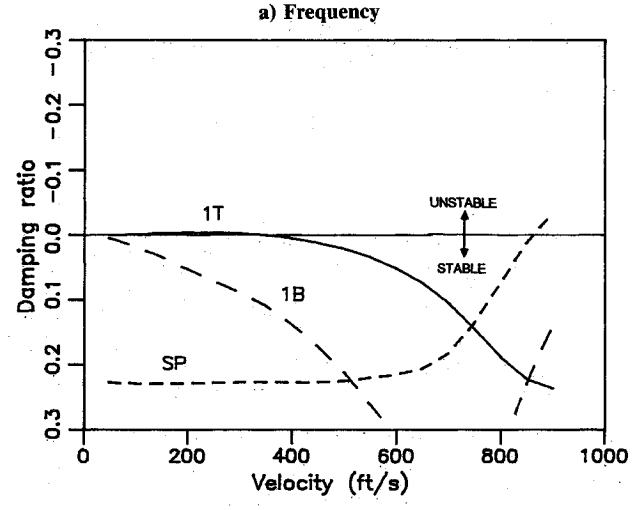


b) Damping ratio

Fig. 7 Free-free aircraft with no blowing.

of $\alpha$ and $C_u$ that results in $C_u$-$\alpha$ stall is most likely to be encountered in STOL or combat-type maneuvers.

Figure 6 shows that, with a high blowing condition, the first bending mode is initially unstable and then, at about 500 ft/s, restabilizes. This phenomenon is due to the negative lift curve slope resulting from the $C_\mu$-$\alpha$ stall condition and is termed CC flutter. The torsion mode is not affected. The variation of modal frequencies with airspeed is not significantly changed when blowing is added and would look similar to that shown in Fig. 5a.

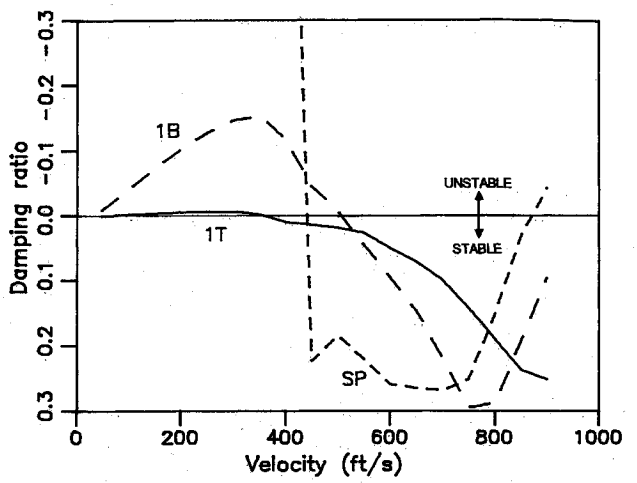


Fig. 8 Damping ratio for free-free aircraft with high blowing.

These results are in agreement with the earlier findings of Haas and Chopra,[10] which showed that CC flutter was a single DOF instability of the first bending mode. However, with the analysis used in Ref 10, the first bending mode did not restabilize at higher speeds, as shown in Fig. 6. This is because $C_\mu$ was assumed to remain constant with airspeed in that study. In the present study, the blowing pressure ratio is held constant, which means that $C_\mu$ will decrease as airspeed increases. As shown in Fig. 3, for the high blowing condition, $C_\mu$-$\alpha$ stall is encountered below $M = 0.5$ and the lift curve slope is negative. At Mach numbers above 0.5, there is insufficient duct pressure available to generate a large $C_\mu$, and the lift curve is positive. It should be noted that CC flutter occurs only in a narrow range of $\alpha$ when sufficient blowing is applied. If the angle of attack is decreased or the blowing level is sufficiently lowered, the $C_\mu$-$\alpha$ stall condition is avoided and CC flutter will not occur.

Stability characteristics of the free-flying aircraft are examined next. Figure 7 shows stability results for the baseline aircraft with no blowing. The first bending and torsion modes follow the same trends as the cantilevered wing. The baseline aircraft configuration has a stable short-period mode (labeled SP in the diagrams) up to about 800 ft/s. At this velocity, the aircraft experiences a body-freedom-flutter (BFF) instability. This instability results from a coupling of the aircraft's short-period mode with the first bending mode of the wing. The coupling arises because of the increasing frequency of the short-period mode with airspeed. (See Ref. 12 for a more complete description of BFF.)

The effects of blowing on stability of the baseline aircraft is demonstrated in Fig. 8. Again, CC wing flutter is encountered with this high blowing condition. Similar to the cantilevered wing, the first bending mode is unstable at low speed and then restabilizes at about 500 ft/s. Comparing the damping in the first bending mode for the free-flying aircraft (Fig. 8) with that of the cantilevered wing (Fig. 6) shows that the CC flutter instability is slightly weaker when rigid-body freedoms are included. Also, with high blowing, the short-period mode of the aircraft becomes statically unstable. This is caused by the negative lift curve slope associated with $C_\mu$-$\alpha$ stall. The short-period mode restabilizes at about 400 ft/s and then follows a trend similar to the aircraft with no blowing. The variation of modal frequencies with airspeed is not significantly changed when blowing is added and would look similar to that shown in Fig. 7a.

The results shown in Fig. 8 indicate the consequences of encountering a condition of $C_\mu$-$\alpha$ stall on the CC wing of free-flying aircraft. First, the wing will begin to flutter at the bending mode frequency. Second, the short-period mode of the aircraft will become unstable. Aircraft instability is less critical because it occurs at a very low frequency, and stability

will quickly be restored as the angle of attack changes or if the blowing level is reduced. The CC flutter instability of the wing is most critical because it occurs at a much higher frequency and could lead to structural failure.

Effects of several aircraft design parameters on the stability of the first wing bending mode are examined for the case when a $C_\mu$-$\alpha$ stall condition exists. In all of the examples presented, the short-period mode of the aircraft will become statically or dynamically unstable with the high blowing level applied. As stated, this is less critical and attention is focused on how design parameters influence the stability of the first bending mode when blowing is applied.

The first design parameter examined is the wing sweep angle. Figure 9 shows the damping in the first bending mode for the cantilevered wing with high blowing at $-45$, 0, and 45 deg of sweep. The results indicate that the aft-swept wing has the weakest instability and confirm the previous findings of Haas and Chopra.[10]

In order to compare the effects of various parameters when aircraft rigid-body motions are included, the wing is attached to the fuselage at the CG point and the horizontal tail is removed unless otherwise stated. Also, the pitch attitude of the aircraft is adjusted to maintain an angle of attack of 4 deg on the wing regardless of sweep angle. The effect of wing sweep including rigid-body motion on flutter stability is shown in Fig. 10, Again, the aft-swept wing encounters the weakest instability. More significantly, if Fig. 10 is compared to Fig. 9, it can be seen that including rigid-body motions weakens the CC flutter instability. For the aircraft with aft-swept wings, 50% less structural damping is required to stabilize the wing

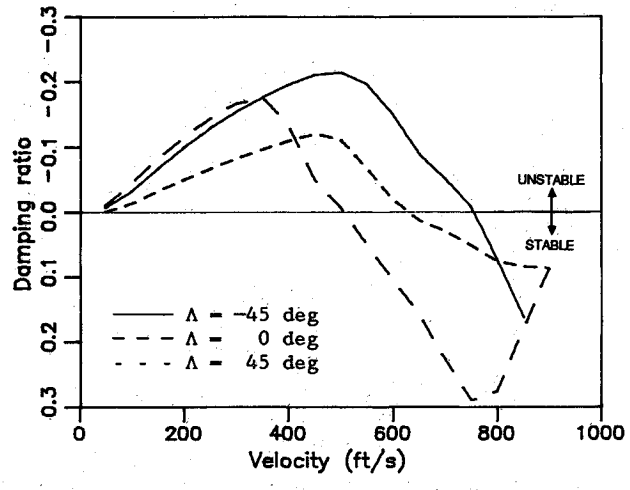


**Fig. 9 Damping in 1B mode for cantilevered wing with high blowing.**

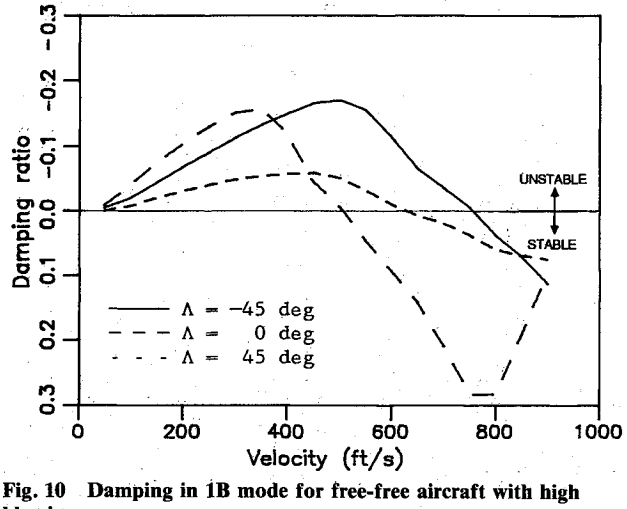


**Fig. 10 Damping in 1B mode for free-free aircraft with high blowing.**

when rigid-body motions are included. The effect of rigid-body freedom is less significant for the straight wing where inertia coupling of the rigid-body modes with the wing elastic modes is minimum.

To further determine the effect of inertia coupling, the fuselage pitch inertia is reduced by 50 and 75% for the aft-swept wing case. Figure 11 shows the effect of reduced pitch inertia on the first bending mode (note the $y$-axis scale change). These results indicate that reducing aircraft pitch inertia considerably weakens the CC flutter instability. In fact, with the baseline inertia reduced by 50% the aft-swept wing aircraft can be stabilized with only 4% structural damping. Results for the forward-swept wing case were also calculated and showed identical trends. Reducing the mass of the fuselage has a similar but less pronounced effect.

Changing the fuselage mass and pitch inertia has a negligible effect when the wing is straight and attached to the aircraft at the CG. This is because inertial coupling of the wing bending mode with aircraft pitch motion is minimal if the wing sweep angle is zero. However, if the wing is mounted away from the aircraft CG, the results change significantly. Several cases with the wing mounted away from the aircraft CG were examined and, regardless of the direction the wing was moved, an improvement in stability resulted.

Inertia coupling of the wing elastic modes with the aircraft rigid-body modes is an important factor in the CC flutter instability of free-flying aircraft. This is clearly shown in Fig. 11 for a configuration where the wing is attached to the fuselage at the CG and no horizontal tail is present. For this configuration, if the wing aerodynamic center is in front of the aircraft CG (forward-swept wing), the aircraft is statically unstable. If the wing aerodynamic center is aft of the CG (aft-swept wing), the aircraft is statically stable. The addition of a high level of blowing changes the statically stable configuration to a statically unstable one and the statically unstable configuration to a dynamically unstable one.

To determine the effect of basic aircraft stability, two complete aircraft configurations with horizontal tails are examined. The first aircraft is identical to the baseline aircraft configuration with a 45-deg aft-swept wing. This configuration is a statically stable design. The second aircraft is identical to the first except for the wing sweep angle of $-45$ deg, which results in a statically unstable aircraft. Damping of the first bending mode for these two cases is shown in Fig. 12 along with earlier results for the wing attached to the fuselage at the CG location with no tail. The addition of the horizontal tail and the aft movement of the wing help to weaken the CC flutter instability of the aircraft with aft-swept wings but have only a negligible influence on the aircraft with forward-swept wings. This is probably because both of these changes increase the stability of the short-period mode of the aft-swept wing

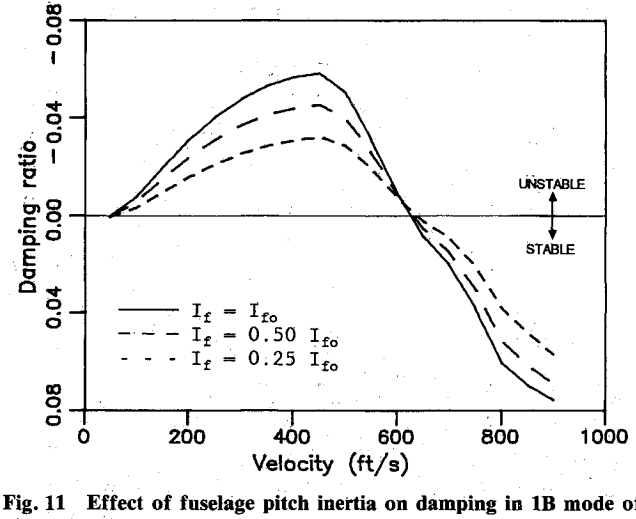


**Fig. 11 Effect of fuselage pitch inertia on damping in 1B mode of aft-swept wing.**

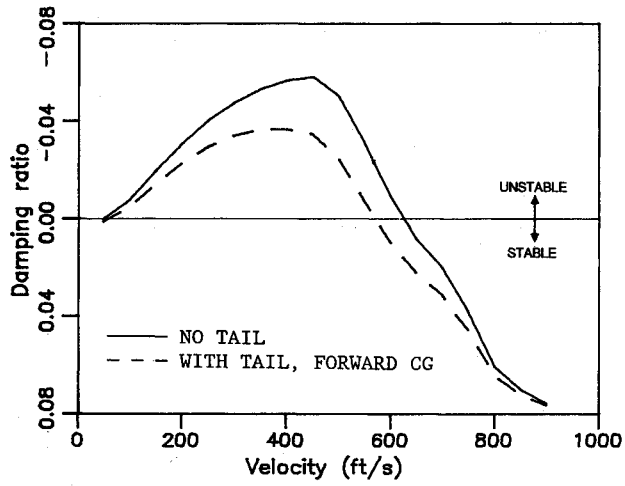


a) Aft-swept wing configuration

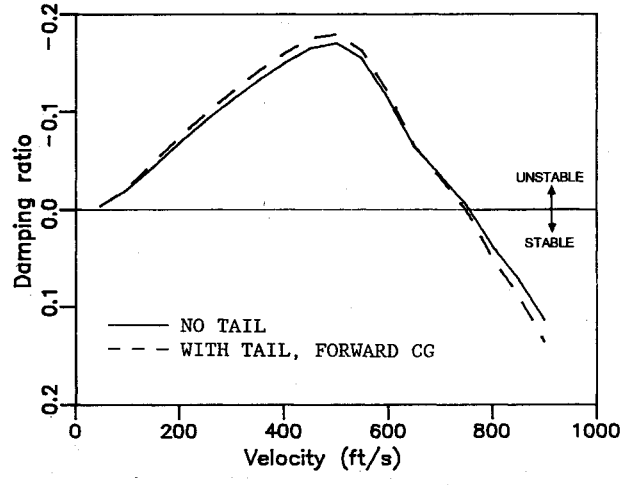


b) Forward-swept wing configuration

**Fig. 12 Effect of horizontal tail.**

aircraft, which in turn helps to stabilize the wing bending mode. In contrast, the forward-swept wing aircraft still remains statically unstable when the tail is added, resulting in a lesser influence on the first wing bending mode.

## Conclusions

Aeroelastic stability of a free-flying aircraft with circulation control wings has been investigated. The primary objective was to determine the effects of rigid-body motion on the CC flutter instability. The flutter analysis is developed for an elastic wing attached to a rigid fuselage undergoing pitch and plunge motions about the center of gravity of the aircraft. A low-speed flutter instability was found on both the cantilevered wing and free-free aircraft when a condition of $C_\mu$-$\alpha$ stall occurred. Based on the parametric study, the following conclusions are drawn:

1) If sufficient blowing is applied to the wing at an angle of attack where the $C_\mu$-$\alpha$ stall condition exists, the wing first bending mode will become unstable for both the cantilevered wing and the wing with rigid-body freedom. This mode restabilizes as velocity increases if blowing pressure ratio remains constant.

2) The CC flutter instability is weakened if the wing is swept aft.

3) Allowing rigid-body motion also weakens this instability due to the inertial relief caused by coupling of the fuselage rigid-body modes with the wing elastic modes.

4) With a high blowing level applied at 4-deg angle of attack, the negative lift curve slope associated with $C_\mu$-$\alpha$ stall causes the aircraft short-period mode to become unstable.

5) Decreasing aircraft pitch inertia for the 45-deg forward- and 45-deg aft-swept wing weakens the CC flutter instability. Decreasing fuselage mass has a similar but less pronounced effect.

6) Changing aircraft mass or pitch inertia for the unswept wing has a negligible effect when the wing is attached to the fuselage at the CG location.

7) The addition of a horizontal tail weakens the CC instability for the statically stable aft-swept wing aircraft but has only a minimal influence on the statically unstable forward-swept wing aircraft.

All of these results indicate that CC flutter will be less severe on a wing if rigid-body pitch and plunge motions are included.

## References

[1]Reader, K. R., Kirkpatrick, D. G., and Williams, R. M., "Status Report on Advanced Development Program Utilizing Circulation Control Rotor Technology," *Vertica*, Vol. 3, No. 1, 1979, pp. 1-23.

[2]Barnes, D. R., Bill, F. A., and Wilkerson, J. B., "Circulation Control Flight Demonstrator Test Program," American Helicopter Society 35th Annual Forum, Washington, DC, May 1979.

[3]Englar, R. F., Trobaugh, L. T., and Hemmerly, R. A., "STOL Potential of the Circulation Control Wing for High Performance Aircraft," *Journal of Aircraft*, Vol. 15, No. 3, 1978, pp. 175-181.

[4]Lane, J. W., and Sumich, M., "The RSRA/X-Wing Experiment, A Status Report," International Powered Lift Conference and Exposition, Santa Clara, CA, Dec. 1987.

[5]Logan, A. H., "Design and Flight Test of the No Tail Rotor (NOTAR) Aircraft," 38th Annual Forum Proceedings of the American Helicopter Society, Anaheim, CA, May 1982.

[6]Schwartz, A. W., Reader, K. R., and Rogers, E. O., "An Unmanned Air Vehicle Concept With Tipjet Drive," Vertical Lift Aircraft Design, Proceedings of the Conference, San Francisco, CA, Jan. 1990.

[7]Englar, R. J., and Applegate, C. A., "Circulation Control—A Bibliography of DTNSRDC Research and Selected Outside References," David Taylor Naval Ship Research and Development Center, Bethesda, MD, DTNSRDC 84/052, AD A146-966, Sept. 1984.

[8]Chopra, I. C., "Aeroelastic Stability of a Bearingless Circulation Control Rotor in Forward Flight," *Journal of the American Helicopter Society*, Vol. 33, July 1988, pp. 60-67.

[9]Haas, D. J., and Chopra, I., "Static Aeroelastic Characteristics of Circulation Control Wings," *Journal of Aircraft*, Vol. 25, No. 10, 1988, pp. 948-954.

[10]Haas, D. J., and Chopra, I., "Flutter of Circulation Control Wings," *Journal of Aircraft*, Vol. 26, No. 4, 1989, pp. 373-381.

[11]Miller, G. D., Wykes, J. H., and Brosnan, M. J., "Rigid-Body Structural Mode Coupling on a Forward Swept Wing Aircraft," *Journal of Aircraft*, Vol. 20, No. 8, 1983, pp. 696-702.

[12]Weisshaar, T. A., and Zeiler, T. A., "Dynamic Stability of Flexible Forward Swept Wing Aircraft," *Journal of Aircraft*, Vol. 20, No. 12, 1983, pp. 1014-1020.

[13]Chen, G. S., and Dugundji, J., "Experimental Aeroelastic Behavior of Forward-Swept Graphite/Epoxy Wings with Rigid-Body Freedom," *Journal of Aircraft*, Vol. 24, No. 7, 1987, pp. 454-462.

[14]Rogers, E. O., Schwartz, A. W., and Abramson, J. S., "Applied Aerodynamics of Circulation Control Airfoils and Rotors," *Vertica*, Vol. 12, No. 1/2, 1988, pp. 69-82.

[15]Nielsen, J. N., and Biggers, J. C., "Recent Progress in Circulation Control Aerodynamics," AIAA Paper 87-0001, Jan. 1987.

[16]Haas, D. J., "Aeroelastic Characteristics of Aircraft with Circulation Control Wings," Ph.D. Dissertation, Dept. of Aerospace Engineering, University of Maryland, College Park, MD, May 1989.

[17]Raghavan, V., Pai, S., and Chopra I., "Circulation Control Airfoils in Unsteady Flow," *Journal of the American Helicopter Society*, Vol. 33, Oct. 1988, pp. 28-37.

[18]Yates, E. C., Jr., "Modified-Strip-Analysis Method for Predicting Wing Flutter at Subsonic to Hypersonic Speeds," *Journal of Aircraft*, Vol. 3, No. 1, 1966, pp. 25-29.

[19]Leishman, J. G., "Validation of Approximate Indicial Aerodynamic Functions for Two-Dimensional Flow," *Journal of Aircraft*, Vol. 25, No. 10, 1988, pp. 914-922.

[20]Leishman, J. G., and Crause, G. L., "A State-Space Model of Unsteady Aerodynamics in a Compressible Flow for Flutter Analysis," AIAA Paper 89-0022, Jan. 1989.